Modelling Radiation Sensor Angular Responses with Dynamic Linear Regression

Ioannis Tsitsimpelis[1], Andrew West[2], Francis R. Livens[2], Barry Lennox[2], C. James Taylor[1*] and Malcolm J. Joyce[1]

***Abstract* — Accurate characterization of radiation hotspots is a critical requirement for monitoring and decommissioning operations in the nuclear industry, particularly where the arrangement of contamination is complex, and the availability of ground-truth data is limited. This article develops a novel stochastic modelling approach that alleviates challenges often present in such operations. Initially, the experimentally derived angular responses of a collimated single detector apparatus at different energy regions (counts over radiation footprints) are expressed by two functions: the Fourier transform of a rectangular pulse (approximated by a sinc function) and a Moffat function. Subsequently, these are both framed within a Dynamic Linear Regression (DLR) model. The resulting Moffat/sinc-DLR models enhance the quality of the fit to experimental data, and improve the accuracy and resolution of radiation localization, thus showcasing the value of such methods for radiation characterization tasks.**

Index terms – radiation detector, source localization, sinc function, Moffat function, dynamic linear regression (DLR)

I. Introduction

Robotic systems are of critical importance in the nuclear industry, because they reduce the need for manned entry into hazardous environments and reduce risks in controlled areas by removing or complementing the human presence [1]. Such robots are equipped with radiation sensing hardware that is appropriately defined based on the task at hand and robotic system requirements, including their size, core instruments, and the estimated radiation hazards in the area for which they are designed to operate.

Single-detector systems, such as the equipment considered in this article, are compact and inexpensive, thus suitable for deployment via various small/medium sized expendable robots [2], [3], [4]. Depending on the configuration used, their signal output can be exploited to both navigate and characterize radioactive areas, e.g. path planning, source seeking and avoidance, source localization and identification, etc. [5], [6], [7]. Mission time constraints, for example due to the battery life of untethered robots, may mandate compromises in the data acquisition process. As a result, localization scans might be carried out with less spatial granularity and/or shorter measurement times than ideal. Hence, in a similar manner to LIDAR data reconstruction via smoothing filters [8], and improving feedback control schemes through functions that represent e.g. sensor reading uncertainties [9], incorporating simple functions to explain radiation data obtained under such constraints, facilitates localization at a finer angular granularity, while also dealing with inherent noise from relatively low-count data. Such functions are subsequently valuable for analysis both on-line (e.g. radiation-seeking exploration) and offline (e.g. for obtaining improved insights about the dispersion of radioactivity within the space analyzed).

The present article focuses on modelling data derived from single-detector localization scans, using time-series methods. It investigates modelling approaches that were proposed in the authors' recent work using the sinc function as the transform method [10], [11], and compares these to new results arising from the use of a Moffat function [12], [13].

The instrumentation used in this research comprises a lead-slit collimated gamma-ray detector, which is mounted on a custom pan-tilt gimbal to enable angular radiation scans of a given environment; and a RedPitaya Field Programmable Gate Array (FPGA) board, configured as a Multi-channel Analyzer (MCA). The hardware occupies a modest physical payload, such that it can be integrated with off-the-shelf mobile robotic platforms (here, the Clearpath Robotics Jackal shown in Fig. 1a). It is operated via the ubiquitous ROS (Robot Operating System) middleware [14], for the purpose of facilitating seamless communication with different robotic subsystems, and for interoperability.

In the presence of ionizing radiation, the shape of the collimated detector's experimental angular response is related inherently to collimation geometry, material, and thickness. Furthermore, it varies with different radiation energies. For the detector-collimator geometry used here, the angular responses can be broadly distinguished in two types. The first, as depicted by the red marks in Fig. 1b, corresponds to pan angle scan responses derived from energy bands below 200 keV (denoted for simplicity as low). The second type, shown

This work was supported in part by the Engineering and Physical Sciences Research Council (EPSRC), under grant EP/V026941/1.

[1] Lancaster University, UK, [2] University of Manchester, UK.
*Correspondence email: c.taylor@lancaster.ac.uk

as black marks in Fig. 1b, corresponds to those derived from energy bands above 200 keV (moderate-to-high). Due to greater attenuation, the former is a better-defined representation of source location and is thus the preferred response to be modelled in straightforward scenarios. However, the utilization of responses for higher energies might also be necessary when, for example, attempting to distinguish different but co-located radionuclides.

The modelling results presented below are formulated based on two illustrative experimental datasets. The low-energy angular responses have been modelled initially by the Moffat function, while the high-energy ones have been modelled by the sinc function. Subsequently, Dynamic Linear Regression (DLR) model estimation techniques [15] have been utilized, aiming to increase the overall accuracy of the simulated equivalent data. The following section II describes the data acquisition and processing steps, as well as the basis and DLR functions; section III presents the modelling results; section IV discusses the findings and further scheduled work; and section V provides the concluding remarks.

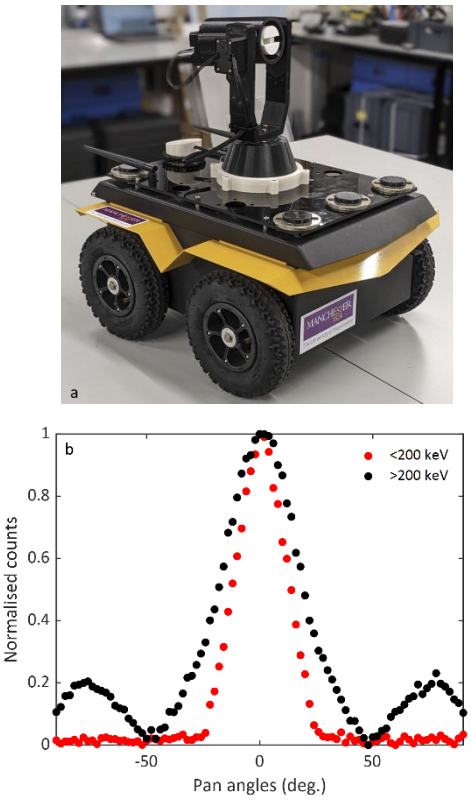

Fig. 1: a) The radiation detection hardware mounted on a Clearpath Robotics Jackal platform; b) Exemplar experimental angular responses, presuming a symmetric horizontal scan with the radiation source located at the centroid of the scan path.

II. Methodology

A. Data collection and processing

The two experimental datasets that are utilized in this paper were obtained as follows. The sources were positioned on a mounting board as depicted in Fig 2a and 2b. The collimated detector was placed at the midpoint of the board, at a distance of 30 cm. With the collimator fixed as a vertical slot, and the tilt angle set to 0°, a symmetric pan angle scan was carried out in 2° intervals (-90° to 90° with 2° intervals – Fig 2c). For each interval, a separate pulse height spectrum was obtained; 91 spectral datasets per experiment. The data were treated with two common post-processing steps: 1) background subtraction to remove cosmic rays and signals that are not part of the actual data (e.g. intrinsic background depending on the detector); 2) gain-drift correction to adjust for variations in detection sensitivity due to angle differences.

The treated spectral collection of each experiment are illustrated in Fig 2d and 2e. Maximum and minimum intensities are represented by yellow and blue colors, respectively. The x-axis represents the MCA channel number, and the y-axis represents the pan angle at which each spectrum was obtained. Each row is essentially a radiation spectrum and each column is an angular response at a particular energy channel. The latter concerns the extracted datasets utilized in this paper, with the low and high energy angular responses that were extracted highlighted in Fig 2d and 2e by red (left hand side) and black (right) dashed traces, respectively.

B. Collimator function: Moffat

The Moffat function is an empirical approximation that displays Lorentzian distribution characteristics (e.g. slow decrease to extremes and shaping parameters with similar effects). It is a point spread function (PSF) and is typically used in imaging applications [13]. The low-energy experimental angular response of a vertical-slot-collimated detector, derived from a horizontal scan along a radioactive source, is formulated on this basis as,

$$y_m(\theta) = m_a + m_b\left(1 + \left(\frac{\theta - m_c}{m_d}\right)^2\right)^{-m_e} \qquad (1)$$

where $y_m(\theta)$ is the detector response (radiation counts) as a function of scan angle θ, and m_a to m_e are fixed coefficients, i.e., m_a is the trend, m_b is the amplitude, m_c determines the centroid position of the peak, m_d controls the width of the curve, and m_e determines the rate with which the amplitude decreases as the distance from the centroid increases. The additional parameters in the Moffat formulism can improve the consistency with which tails and wings of an angular response are reproduced and is thus more flexible than a Gaussian distribution for this application.

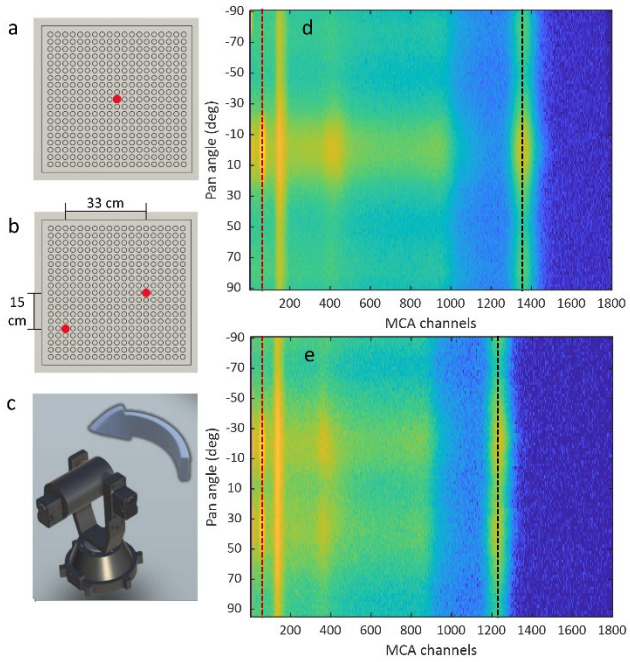

Figure 2: a-b) Depictions of source placement in each experiment; c) Depiction of the gimbal scan action over the horizontal plane with zero tilt; d-e) Post-processed radiation spectra over different angles, presented as 2D images. The dashed columns represent the angular responses extracted for this paper.

C. Collimator function: Sinc

The high-energy experimental angular responses are best approximated in this work by a sinc function [10], [11], constructed observationally as:

$$y_s(\theta) = s_a + s_b\left(\frac{\sin(s_c(\theta - s_d))}{s_c(\theta - s_d)}\right) \quad (2)$$

where $y_s(\theta)$ is the detector response (radiation counts) as a function of scan angle θ, and s_a to s_d are coefficients, i.e., s_a is the trend, s_b is related to the amplitude, s_c determines its width, and s_d corresponds to the curve's peak location.

D. Moffat-DLR and sinc-DLR models

The aim of utilizing a DLR model is to improve the overall fit of the angular response, so that situations where the source arrangement is not known might be characterized more effectively. Adapted from [15] for the present application:

$$y_{DLR}(k) = p_1(k)x_1(k) + p_2(k)x_2(k) + e(k) \quad (3)$$

where $y_{DLR}(k)$ is the simulation output for sample k, $p_1(k)$ and $p_2(k)$ are angle variant parameters, $x_1(k)$ and $x_2(k)$ are the associated regressors for the varying parameters, and $e(k)$ is Gaussian white noise. For both Moffat-DLR and sinc-DLR representations, the regressor $x_1(k)$ is set to unity. For the Moffat-DLR model, regressor x_2(k) is formed from the curve-shaping part of Eq. 1, i.e., $x_2(k) = \left(1 + \left(\frac{\theta(k) - m_c}{m_d}\right)^2\right)^{-m_e}$. In the sinc-DLR case, x_2(k) introduces the sinc component of Eq. 2, i.e., $x_2(k) = \frac{sin(s_c(\theta(k) - s_d))}{s_c(\theta(k) - s_d)}$. In both cases, an expected shape and peak location of the simulated response is imposed on the model, while the trend and slope in Eq. 3 are the time-varying (in this case varying with angle) equivalents of m_a and m_b in Eq. 1, and s_a and s_b in Eq. 2. The Moffat-DLR and sinc-DLR models are thus defined as follows:

$$y_{mDLR}(k) = p_{1m}(k) + p_{2m}(k)\left(1 + \left(\frac{\theta(k) - m_c}{m_d}\right)^2\right)^{-m_e} + e(k) \quad (4)$$

$$y_{sDLR}(k) = p_{1s}(k) + p_{2s}(k)\left(\frac{sin(s_c(\theta(k) - s_d))}{s_c(\theta(k) - s_d)}\right) + e(k) \quad (5)$$

The angle-variant parameters are each represented by an Integrated Random Walk model, expressed in stochastic state space form for estimation purposes. The states (and hence parameters) are estimated using Kalman filtering and fixed-interval smoothing algorithms, implemented in MATLAB via the CAPTAIN Toolbox [16].

III. Model Estimation Results

A. Low energy angular responses

Fig. 3a shows data from the single-source experiment (black circles), simulation outputs from Eqs. 1 (blue) and 4 (red), and the associated standard errors (SE). The coefficients of Eq. 1 are calculated using the optimization toolbox in MATLAB, with parameter values estimated as follows: $m_a = 0.0063$, $m_b = 1$, $m_c = 0.6394$, $m_d = 25$ and $m_e = 3.3306$.

The metric for evaluating the simulation outputs is R^2, since it focuses on a key point of interest here, i.e. how well each model explains the variance in the data. R^2 for the Moffat simulation is 0.9928 while the Moffat-DLR equivalent is 0.9988, suggesting a marginal improvement. This is evident by the corrected response in the regions between 20° to 40° and -20° to -40°. Figs. 3b-c show the Moffat-DLR parameters and standard errors. The trend parameter, $p_{1m}(k)$, exhibits negligible variation and uncertainty, whilst the slope parameter, $p_{2m}(k)$, is more consistent between circa 40° and -40° but exhibits large uncertainty outside these angles.

Fig. 4 concerns results from the experiment with two radioactive sources. In this case, an individual Moffat function is modelled for each of the two peaks, while the Moffat-DLR model takes the following form:

$$y_{mDLR}(k) = p_{1m}(k) + p_{2m}(k)\left(1 + \left(\frac{\theta(k) - m_c}{m_d}\right)^2\right)^{-m_e} + p_{3m}(k)\left(1 + \left(\frac{\theta(k) - m_h}{m_i}\right)^2\right)^{-m_j 2} \quad (6)$$

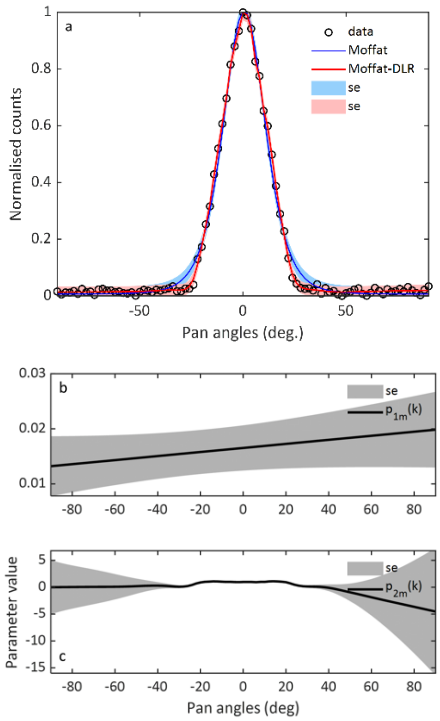

Figure 3: a) Experimental data and model fits from Moffat and Moffat-DLR models, and SEs; b) Eq. 4 trend parameter variation and SE; c) Eq. 4 slope parameter variation and SE.

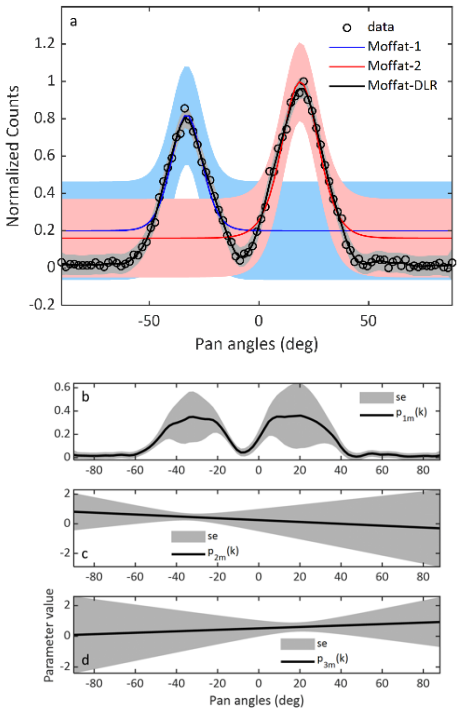

Figure 4: a) Experimental data, model fits from Moffat and Moffat-DLR models, and SEs; b-d) Eq. 6 parameter variations and SEs.

Fig. 4a displays the experimental data points, along with the individual results of the Moffat simulations, the Moffat-DLR output based on Eq. 6, and the standard errors for each simulation. The coefficients for each individual Moffat function are given in Table 1. Here, the coefficients for the second peak are denoted m_f to m_j, equivalent to m_a to m_e for the first. The R^2 value of the Moffat-DLR fit is 0.9944.

Figs. 4b-d show the Moffat-DLR parameters and standard errors. The intercept in this instance exhibits a relatively high variability around the curve regions, while $p_2(k)$ and $p_3(k)$ display a linear decrease and increase, respectively. It is also overt that for each parameter, their estimated values show more certainty around their respective region of operation (i.e. baseline for intercept, left and right peak for the slopes).

B. High-energy angular responses

The high-energy angular responses are modelled here with a sinc function, and subsequently via sinc-DLR. Fig. 5a depicts the data and simulation outputs from Eqs. 2 and 5, and the standard errors. Using the MATLAB curve fitting toolbox, the coefficients of Eq. 2 are: $s_a = 0.1509$, $s_b = 0.7748$, $s_c = 0.0983$, and $s_d = -0.5886$. The R^2 values for the sinc and sinc-DLR simulation are 0.9688 and 0.9988, respectively. The sinc-DLR response yields an improved fit to the data, including for the peak, baseline and side lobe regions.

Figs. 5b-c, show the sinc-DLR parameters and standard errors. Parameter $p_{1s}(k)$ exhibits an arc-shaped trend with low SEs, while $p_{2s}(k)$ exhibits large uncertainty for estimated values on the extreme ends.

For the two-source experiment, similar to Eq. 6, the sinc-DLR model takes the following form:

$$y_{sDLR}(k) = p_{1s}(k) + p_{2s}(k)\left(\frac{\sin(s_c(\Theta(k)-s_d))}{s_c(\Theta(k)-s_d)}\right) + p_{3s}(k)\left(\frac{\sin(s_g(\Theta(k)-s_h))}{s_g(\Theta(k)-s_h)}\right) \quad (7)$$

Fig. 6a depicts the experimental angular responses, the individual sinc simulations based on Eq. 2, the sinc-DLR output based on Eq. 6, and the standard errors for each simulation. The color codes are consistent with the previous figures. The coefficients for each individual sinc function are given in Table 2. The individual model fits exhibit, as expected, a poor capture. However, by including information for both peaks on the structure of the sinc-DLR model, the resulting fit captures the variation of the experimentally-derived radiation counts along the measurement space accurately ($R^2 = 0.9965$). Finally, Figs. 6b-d depict the sinc-DLR angle variant parameters and SEs, exhibiting a broadly similar behavior to that observed for the Moffat-DLR describing the low-energy angular responses.

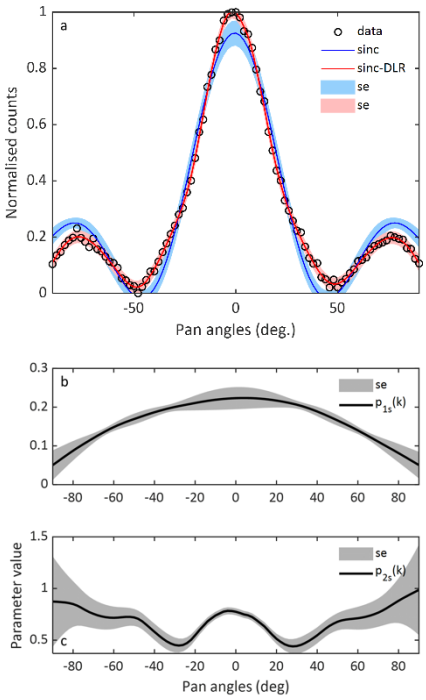

Figure 5: a) Experimental data and model fits from sinc and sinc-DLR models, and SEs; b) Eq. 5 trend parameter variation and SE; c) Eq.5 slope parameter variation and SE.

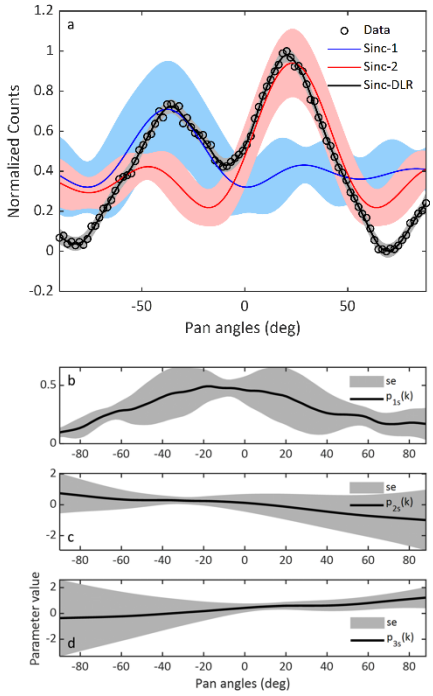

Figure 6: a) Experimental data, model fits from sinc and sinc-DLR models, and SEs; b-d) Eq. 6 parameter variations and SEs.

Moffat-1	m_a	m_b	m_c	m_d	m_e
	0.1993	0.6212	-32.9555	25	6.7397
Moffat-2	m_f	m_g	m_h	m_i	m_j
	0.1593	0.8403	18.778	25	4.83

Table 1: Individual Moffat function coefficients.

sinc-1	s_a	s_b	s_c	s_d
	0.3898	0.3201	0.1163	-37.73
sinc-2	s_e	s_f	s_g	s_h
	0.3469	0.5944	0.1102	23.19

Table 2: Individual sinc function coefficients.

IV. Discussion

Estimating models using time-series techniques applied to spatial data, as presented here, shows promise in robotic-enabled radiation characterization tasks. Raw data have been processed within a time-series model estimation framework to improve source localization. Casting the sinc and Moffat functions into the DLR model form, yields general improvements in fitting the experimental data.

For example, in Fig. 3a, the Moffat-DLR model corrects the tail settling deviations observed by the Moffat function alone; and in Fig. 5a, the sinc-DLR hits all the data regions not captured accurately by the sinc function. For the other experiment, where two radiation sources are involved, both DLR models reproduce the experimental data more consistently, but the parameter standard errors are locally very large or small. While the sinc-DLR model in Fig. 6a captures all the data accurately, the Moffat-DLR output in Fig. 3a displays a deviation from the true amplitude of the peaks. In its current form, an attempt to improve the model fit such that the model would also explain the true amplitude of the peaks, results in overfitting and much larger standard errors in the parameters.

The broader merit of these functions is that, in addition to the localization capability, it is possible to utilize them for distinguishing complex features that are typical in real-world characterization scenarios, such as identifying a false response arising from radiation scattering (an analogy to this would be false localization due to a mirror in the field of view of a camera).

In terms of the functions utilized within the DLR framework, it is observed that the curve-shaping parameters are fixed constant and hence the DLR model can only vary the scaling components to optimize the fit. A variation of this framework in which all parameters are allowed to vary could be useful, i.e., for minimizing the total number of parameters, since this approach would discard the need to include an additional sinc/Moffat component for each peak.

Ongoing research by the authors involves investigating this and further options within the general DLR framework (e.g., choice of regressors, parametric efficiency with increasing peaks, use of other time-series models, etc.).

Future research will also evaluate formal spatial autoregressive models that directly incorporate spatial dependencies due to collimation and radiation source geometries.

V. Conclusions

This article has presented results from modelling radiation detector spatial responses, combining sinc and Moffat components with a statistical DLR approach. The resulting Moffat/sinc-DLR models explain the experimental data satisfactorily and are thus appropriate to incorporate into radiation characterization tasks, particularly where the arrangement of contamination is complex, and the availability of ground-truth data is limited. Future articles will report on a systematic comparison with other modelling techniques, using data for a wider range of radiation scenarios.

VI. References

[1] I. Tsitsimpelis, C. J. Taylor, B. Lennox, and M. J. Joyce, "A review of ground-based robotic systems for the characterization of nuclear environments," *Progress in Nuclear Energy*, vol. 111, pp. 109–124, 2019.

[2] W. Cheah, K. Groves, H. Martin, H. Peel, S. Watson, O. Marjanovic, and B. Lennox, "MIRRAX: A reconfigurable robot for limited access environments," *IEEE Transactions on Robotics*, vol. 39, pp. 1341–1352, 2023.

[3] A. Miller, R. Machrafi, and A. Mohany, "Development of a semi-autonomous directional and spectroscopic radiation detection mobile platform," *Radiat Meas*, vol. 72, pp. 53–59, 2015.

[4] A. West, B. Lennox, I. Tsitsimpelis, M. Aspinall, M. J. Joyce, P. Coffey, P. A Martin, and N. Smith, "TORONE: Total Characterisation by Remote Observation of Nuclear Environments – 20591," *WM2020: Annual Waste Management Conference,* 2020.

[5] A. West, T. Wright, I. Tsitsimpelis, K. Groves, M. J. Joyce, and B. Lennox, "Real-time avoidance of ionising radiation using layered costmaps for mobile robots," *Frontiers in Robotics and AI*, vol. 9, 862067, 2022.

[6] A. West, I. Tsitsimpelis, M. Licata, A. Jazbec, L. Snoj, M. J. Joyce, and B. Lennox, "Use of Gaussian process regression for radiation mapping of a nuclear reactor with a mobile robot," *Scientific Reports*, vol. 11, 13975, 2021.

[7] I. Tsitsimpelis, A. West, M. Licata, M. D. Aspinall, A. Jazbec, L. Snoj, P. A. Martin, B. Lennox, M. J. Joyce, "Simultaneous, robot-compatible γ-ray spectroscopy and imaging of an operating nuclear reactor," *IEEE Sensors Journal*, Vol. 21, pp. 5434-5443, 2021.

[8] T. Yun, K. Jiang, G. Li, M. P. Eichhorn, J. Fan, F. Liu, B. Chen, F. An, and L. Cao "Individual tree crown segmentation from airborne LiDAR data using a novel Gaussian filter and energy function minimization-based approach," *Remote Sens Environ*, vol. 256, p. 112307, 2021.

[9] A. Hakobyan and I. Yang, "Wasserstein Distributionally Robust Motion Control for Collision Avoidance Using Conditional Value-at-Risk," *IEEE Transactions on Robotics*, vol. 38, pp. 939–957, 2022.

[10] I. Tsitsimpelis, T. L. Alton, A. West, C. J. Taylor, F. R. Livens, B. Lennox, and M. J. Joyce, "Improved localization of radioactivity with a normalized sinc transform," *Frontiers in Nuclear Engineering*, vol. 1, 862067, 2022.

[11] I. Tsitsimpelis, T. Alton, A. West, C. J. Taylor, B. Lennox, F.R. Livens, and M. J. Joyce, "Localising and identifying radionuclides via energy-resolved angular photon responses," *Nucl Instrum Methods Phys Res A*, vol. 1057, p. 168771, 2023.

[12] A. F. J. Moffat, "A theoretical investigation of focal stellar images in the photographic emulsion and application to photographic photometry.," *Astronomy and Astrophysics,* vol. 3, pp. 455–461, 1969.

[13] S. C. Elísio, A. Bala, M. Bandala, J. Graham, A. Grievson, and M. J. Joyce, "Point-spread analysis of γ-ray/depth spectra for borehole monitoring applications," *IEEE Trans Nucl Sci*, vol. 70, pp. 2506–2514, 2023.

[14] M. Quigley, B. Gerkey, K. Conley, J. Faust, T. Foote, J. Leibs, E. Berger, R. Wheeler, A. Ng, "ROS: an open-source Robot Operating System," *ICRA workshop on open source software*, 2009.

[15] P. Young, "Data-based mechanistic modeling of engineering systems," *Journal of Vibration and Control*, vol. 4, pp. 5–28, 1998.

[16] C. J. Taylor, P. C. Young, W. Tych, and E. D. Wilson, "New developments in the CAPTAIN Toolbox for Matlab with case study examples," *IFAC–PapersOnLine*, vol. 51, pp. 694–699, 2018.